Spatial Correlation in Indoor Massive MIMO: Measurements and Ray Tracing

Sergei Shikhantsov, Andrea Guevara, *Student Member, IEEE*, Arno Thielens, *Member, IEEE*, Günter Vermeeren, *Member, IEEE*, Piet Demeester, *Fellow, IEEE*, Luc Martens, *Member, IEEE*, Guy Torfs, *Senior Member, IEEE*, Sofie Pollin, *Senior Member, IEEE*, and Wout Joseph, *Senior Member, IEEE*

***Abstract*—This letter investigates spatial correlation properties of radio-frequency massive multiple-input–multiple-output (MIMO) channels. The correlation between channel vectors at the receive side is studied for the interreceiver distances up to several wavelengths. This is an important property of 5G wireless networks and its accurate prediction is desirable in many applications. Measured and simulated channels are compared using an alternative formulation of the channel correlation function, the argument of which is the distance between any two receivers in proximity of a selected region. The measurements were conducted using a massive MIMO base station (BS) testbed and virtual arrays of receivers, positioned with a robotic system. The simulations were performed using the ray-tracing (RT) technique in a simplified model of an indoor environment, augmented with stochastic geometry elements. In addition, a line-of-sight (LOS) channel model was derived from the RT results, and the role of the scattered power on the correlation was evaluated. The results show that the RT model predicts the correlation with an error not exceeding 10%. The variation of the correlation function profile with increasing receiver to BS separation distance is also captured by the RT model. The simulated LOS model predictions, which account solely for direct propagation paths, were found to significantly underestimate the correlation at the subwavelength distance, and overestimate it at larger distances.**

***Index Terms*—Channel characterization, correlation, massive multiple-input–multiple-output (MIMO), ray tracing (RT).**

I. Introduction

MASSIVE multiple-input–multiple-output (MIMO) [1] is widely accepted as a 5G technology [2]. The massive MIMO down-link (DL) *transmission precoding* aims at elevating the signal strength at the antenna terminals of the intended receivers (Rx). Traditional beam-forming techniques operate in the direction-of-departure (DOD) space, increasing the base station (BS) array pattern directivity toward the intended Rx. In contrast to that, the massive MIMO precoding operates in the channel space, setting the BS array transmit vector according to the Rx receive vector. This leads to the formation of spatial regions with increased electromagnetic field (EMF) levels around the Rx antenna locations [3], further referred to as *hotspots*. Concentrating EMF values in a hotspot reduced potential unwanted spatial interference between different RX locations.

A large number of elements in the BS array and precoded transmission ensure that the EMF strength decreases with distance from the intended Rx, as the observed channel vector becomes less similar to the one at the Rx location. The rate at which the correlation between two Rx channels decreases with the distance between them, determines the size of the hotspot. This size dictates the distance at which two receivers can be spatially multiplexed. Spatial multiplexing is desirable because it increases throughput in a network. Additionally the ability to predict a hotspot size could be demanded by many practical applications, e.g., wireless power harvesting or studies of the human electromagnetic exposure.

The correlation properties at the transmitter (Tx) side are studied extensively in the literature from analytical [4] and experimental [5] standpoints. The Rx side received less attention so far. Relevant information can be found in [6], where performance of a wireless power harvesting beacon was studied. From these results, we estimate the hotspot cross-section radius to be around 0.3 m, or 3 λ at 2.6 GHz and 1.6 m Tx–Rx separation distance. In [7] and [8] the hot-spot power density distribution was modeled as an interference pattern of a large number of plane-waves incident at the Rx. The hostspot size was around 1 λ (86 mm) at 3.5 GHz. Relevant results are found in the COST 2100 model [9] study of the temporal autocorrelation function of moving users in line-of-sight (LOS) 64-antenna element massive MIMO channels at 2.6 GHz. The correlation coefficient rapidly dropped to around 0.5 at a distance of approximately 0.1 m (1λ), and remained at the same level at larger distances. In [10], scalar products of channel vectors measured at 5.8 GHz are reported for users in LOS at approximately 15 m distance from a 64-element BS. The scalar product was around 0.4 for 0.2 m (4λ) between users and dropped to nearly 0.2 at 1 m (20λ).

This contribution, for the first time to the authors' best knowledge, studies the spatial correlation properties of massive MIMO

Manuscript received February 11, 2021; accepted March 5, 2021. Date of publication March 17, 2021; date of current version June 2, 2021. This work was supported in part by the Excellence of Science (EOS) project MUlti-SErvice Wireless NETworks (MUSE-WINET). The work of Piet Demeester was supported by the ERC under Grant 695495 "ATTO: A new concept for ultra-high capacity wireless networks." The work of Andrea P. Guevara was supported by the European Union's Horizon 2020 under Grant Agreement 732174 (ORCA project). The work of Arno Thielens was supported by the Research Foundation - Flanders (FWO) under Grant 1283921N. *(Corresponding author: Sergei Shikhantsov.)*

The authors are with the Department of Information Technology, Universiteit Gent, 9000 Gent, Belgium (e-mail: sergei.shikhantsov@ugent.be; aguevara@esat.kuleuven.be; arno.thielens@ugent.be; Gunter.Vermeeren@UGent.be; Piet.Demeester@UGent.be; luc.martens@intec.ugent.be; Guy.Torfs@UGent.be; sofie.pollin@esat.kuleuven.be; Wout.Joseph@UGent.be).

Digital Object Identifier 10.1109/LAWP.2021.3066607

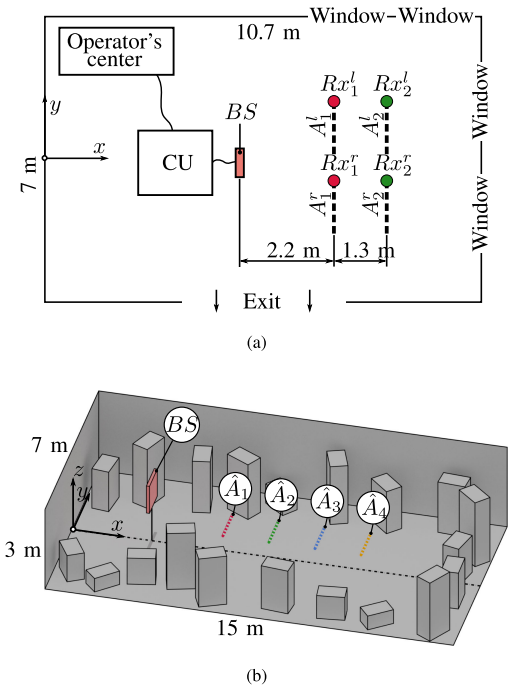

Fig. 1. (a) Top view of the measurement environment. The BS is shown with a red rectangle, two Rx tracks are shown with dashed lines. (b) RT environment sample. The BS is shown with a pink box, while the dashed colored lines indicate the locations of $A_i, i \in \{1, 2, 3, 4\}$ in the simulation.

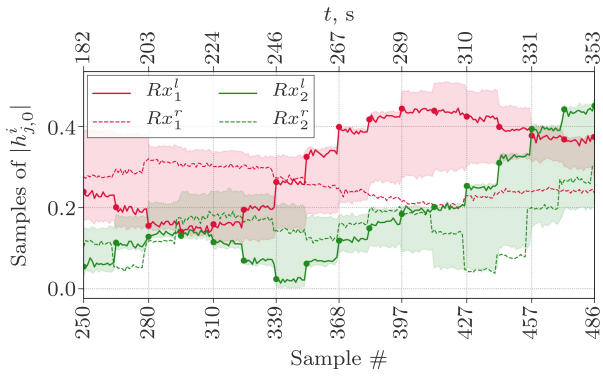

Fig. 2. Channel magnitudes at the first BS element (2.61 GHz subcarrier) as the Rx antennas pass through 16 stationary locations are shown with solid and dashed lines. Bottom axis tracks the channel sample number, top axis - time since the first measured sample. Shaded regions show the channel magnitude $\min - \max$ range across all 100 subcarriers. Channels of Rx_1 and Rx_2 are shown in red and green, respectively.

at the Rx side, comparing measured and simulated channels. The measurements were conducted using a massive MIMO test-bed with 64 elements [5] (KU Leuven, Belgium), operating at the center frequency of 2.61 GHz. The simulations were performed using the ray-tracing (RT) method in a synthetic environment, approximating the one in which the measurements were taken. The RT method is widely and successively used for indoor massive MIMO channel modeling in [11]. The RT method accurately predicts the directional spread of diffuse multipath propagation [12]—the key mechanisms connecting the receivers' correlation and their positions in the environment. The main contribution of this letter is the validation of the RT approach for prediction of the correlation properties of massive MIMO channels. The measurement setup presented in the next section aims to model an indoor LOS scenario [13] in which UEs are autonomous mobile robots [14]. Such setting is one of the major anticipated industrial 5G applications in "Industry 4.0" [15] or "Factories of the Future" [16].

In addition, to evaluate the multipath contribution we studied pure LOS channels, derived from the RT simulations. The effect of the environment on the correlation profile was quantified by comparing the LOS and measured channels at different distances from the BS.

II. Materials and Methods

A. Measurements

A top view of the measurement setup is shown schematically (to scale) in Fig. 1(a). The KU Leuven massive MIMO testbed is a TDD-LTE-based system controlled by the MIMO Application Framework of National Instruments, with a center frequency of 2.61 GHz. The testbed comprises two parts, the BS and user equipment (Rx). The BS is equipped with $N = 64$ dual-band patch antennas, located as a planar array of 8-by-8 elements. For the user equipment a single dipole antenna is used per data stream. The center of the BS array is located at $x = 5$ m, $y = 0$ m, $z = 1$ m in the coordinate system depicted in Fig. 1(a).

Two pairs of Rx antennas, (Rx_1^l, Rx_1^r) and (Rx_2^l, Rx_2^r) in Fig. 1(a), are each mounted on a positioning system 2.2 and 3.5 m shortest distance from the plane of the BS, 0.3 m above the ground. The positioning systems are controlled from the operator's center [Fig. 1(a)]. Simultaneously, they move the Rx antennas parallel to the y-axis. Rx_1^l and Rx_2^l are moved from $y = 1.45$ m to $y = 0.17$ m, and Rx_1^l and Rx_2^l are moved from $y = -0.17$ m to $y = -1.45$ m (1.28 m of movement range for each Rx). After each 10 mm traveled, the positioners halt the motion for 10 s to allow the BS control unit (CU) to record enough channel state samples, resulting in $K = 129$ fixed positions per Rx. The positioners report the local coordinates of each halted Rx and the Network Time Protocol (NTP) timestamp [17] at the moment it arrives at the location.

Fig. 2 shows the channel coefficients' $(h_{j,0}^i)$ absolute values measured at one of the BS elements (with index 0) for 16 consecutive fixed Rx positions. Red and green colors in Fig. 2 show channels to Rx_j^l and $Rx_j^r, j \in \{1, 2\}$, respectively. Lines depict the channel magnitudes for the subcarrier with the center frequency of 2.61 GHz, and the shaded regions show the minimum–maximum range across all subcarriers. Solid dots mark the channel values at the NTP timestamps which have the smallest time difference with the timestamps reported by the positioning system.

The channel magnitude shows a staircase-like behavior; periods with relatively stable values are followed by abrupt jumps, forming an alternating pattern. The stable periods correspond to the time instances when the Rx antennas are static and the channel variation is caused by thermal noise or changes in the environment. Rapid jumps of the channel always occur when the Rx antennas are moved from one stationary location to another. This can be seen from the positioner NTP timestamps in Fig. 2 (marked with solid dots) which follow these jumps.

It should also be noted that none of the channel sample series are correlated between receivers (absolute value of the Pearson's correlation coefficient ≤ 0.02.), which is expected, as Rx are separated by over 1 m (around 7λ) distance at any time instance. The amount of time it takes for the Rx to be moved from one stationary position to another is below 0.5 s and at most a single channel sample can be measured by the BS CU during this time period. These samples are undesirable and therefore excluded from further analysis.

Each stationary Rx position is treated as an element of a virtual array of receivers with channel matrices $H_j^i \in \mathbb{C}^{N\times K}, j \in \{1,2\}, i \in \{l,r\}$. The matrix element $h_{j,kn}^i$ of H_j^i is then defined as the arithmetic mean of the channel coefficient samples measured between the BS element n and the Rx_j^i at the location k. The average relative standard error of both real and imaginary parts of $h_{j,kn}^i$ (ripple of the channel samples with stationary Rx) is around 3% and is much smaller than its variation across the subcarriers.

B. Ray Tracing

The RT simulations were conducted with the Wireless InSite 3.3 (REMCOM) software suite. Environment geometry, dielectric material properties, Tx, and Rx positions are the input for the RT solver at 2.61 GHz.

1) Model of the Environment: The RT geometry is contained within a single cuboid (the floorplan). Its sides are aligned with the coordinate axes. In addition, scatterers are distributed randomly inside the floorplan to diversify the propagation. The scatterers are nonintersecting cuboids of a fixed footprint. Their centers are positioned in the horizontal plane using the Poisson disc sampling algorithm [18] within a 2 m distance from the nearest wall inside the room. Each scatterer is rotated around the vertical axis, that passes through its center, at an angle, sampled independently from the uniform distribution in $[0, 2\pi]$. A geometry with defined scatterer positions is further referred to as *environment sample*.

One of the simulated environment samples is depicted in Fig. 1(b). The coordinates of the BS center and relative positions of its antenna elements match those used during the measurements. The Rx arrays are shown with solid colored lines in Fig. 1(b). The $\hat{A}_1$ and $\hat{A}_2$ arrays have the same coordinates as the measured A_1^l and A_2^l. The $\hat{A}_3$ and $\hat{A}_4$ arrays have the same y and z coordinates, but are shifted along the x-axis to $x = 9.8$ m and $x = 11.1$ m, respectively. Indexed this way, the larger the index of an array, the larger the distance of this array from the BS.

The y- and z- dimensions of the room are equal to the corresponding dimensions of the measurement site (7 and 3 m, respectively). The room size in the x direction was extended to 15.5 m (compared to 10.7 m of the measurement site), in order to fit the A_3 and A_4 arrays into the simulation domain. All geometric entities are assigned identical dielectric properties $\varepsilon_r = 7,\ \sigma = 1.5 \cdot 10^{-2}$ S/m, modeling concrete material [19].

Vertically polarized half-wave dipole patterns are assigned to the antennas of all BS array elements and receivers. Transmitters are excited with a continuous sinusoidal signal with frequency $f_c = 2.61$ GHz (the test-bed center frequency).

2) Channel Matrix Calculation: The ray tracer calculates the channel coefficient between the nth BS antenna element and kth Rx location as

$$\hat{h}_{j,kn} = \sum_{r\in s_j(n,k)} u_r \exp(-2\pi i f_c \tau_r) \tag{1}$$

where j is the virtual array index, $s_j(n,k)$ is the set of indices of rays found for the (n,k) Tx–Rx pair, u_r is the amplitude of the voltage induced by the ray r at the Rx antenna terminal and τ_r is the time-of-flight of the ray r. The RT channel matrix $\hat{H}_j$ is obtained by evaluating (1) for each Tx–Rx pair in the BS and the A_j.

C. Free-Space Line-of-Sight Model

It is possible to modify (1), such that only the direct paths between the Tx–Rx pairs are accounted for. Replacing $s_j(n,k)$ with the LOS ray $r_{j,kn}^{\text{LOS}}$ (the LOS path exists for all Rx locations in the studied scenario), we obtain the free-space LOS (FS-LOS) channel coefficients

$$h_{j,kn}^{\rightarrow} = u_r \exp(-2\pi i f_c \tau_r)|_{r_{j,kn}^{\text{LOS}}} \tag{2}$$

that form the channel matrix $H_j^{\rightarrow}$.

D. Channel Equalization

To exclude the effect of the path loss (PL) we equalize the channel vectors. This is achieved by multiplying the channel matrix by the vector of its inverse column norms. For any channel matrix H

$$\bar{H} = [\|\mathbf{h}_0\|^{-1}, \|\mathbf{h}_1\|^{-1}, \ldots, \|\mathbf{h}_K\|^{-1}]H \tag{3}$$

where $\mathbf{h}_k = [h_{k0}, h_{k1}, \ldots, h_{kN}]^T$ is the kth channel vector.

Equalization (3) removes the channel magnitude variation, but preserves the BS antenna amplitude and phase ratios.

E. Spatial Correlation Function

The equalized channel correlation matrix is defined using the equalized channels as

$$G = \bar{H}\bar{H}^{*T}. \tag{4}$$

As $g_{kk} = \bar{h}_k \bar{h}_k^{*T} = \|\bar{h}_k\| = 1$, any diagonal element of G equals to unity, as a norm of the equalized channel vector. The absolute value of the off-diagonal element g_{kl} is the signal magnitude received by the lth Rx, when the BS transmits to the kth Rx using the maximum ratio transmission (MRT) precoding, with signal fading variation removed. This is proportional to the interference between the kth and lth Rx locations, assuming the MRT precoding.

As the distance between any two consecutive Rx positions is constant ($\delta = 10$ mm), the absolute values of the elements on the l-diagonal of G are also the interference signals received by the elements separated by distance $\Delta(l) = l \cdot \delta$. Therefore, we define a correlation function $\rho_j(\Delta)$, the argument of which is the distance $\Delta(l)$ between *any* two Rx locations in A_j, as the arithmetic mean of the absolute values of the elements on the lth diagonal of G_j

$$\rho_j(\Delta) = \frac{\sum_{i=1}^{K-l} |g_{i,i+l}^j|}{K-l} \tag{5}$$

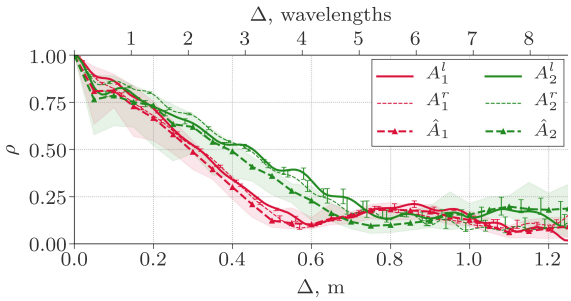

Fig. 3. Correlation function ρ calculated using measured and simulated channels. ρ_1 and ρ_2 are shown with red and green color, respectively. The RT channels are shown with dashed triangle marker lines and shaded regions depict $\min - \max$ range over the 25 environment samples. The measured channels are shown with solid and doted lines for A_j^l and A_j^r, respectively, and error-bars show 5–95 percentile range over subcarriers.

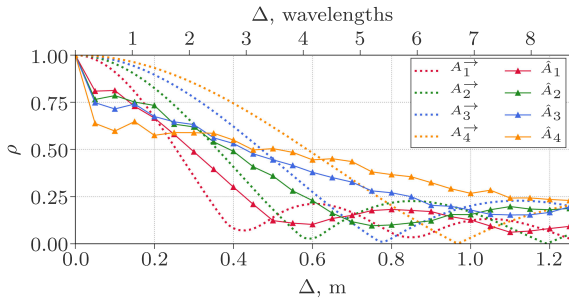

Fig. 4. Correlation function RT/FS-LOS comparison. Graphs of $\hat{\rho}$ for full RT and FS-LOS channels are shown with solid and dotted lines, respectively. The line colors matches the color of the arrays shown in Fig. 1(b).

where $g_{k,l}^j$ is the element of G^j. Due to the channel equation (3), $\rho(0) = 1$, which means that the channel of any element is fully correlated with itself. If $\rho(\Delta) = 0$, then all elements separated by the distance d_l are pairwise fully decorrelated, that is, their channel vectors are orthogonal. From (4) and (5) it also follows that $\rho_j(\Delta)$ is an estimate of the average normalized power received at the distance $\Delta(l)$ from the intended receiver parallel to the Rx array. Thus, the correlation function can be viewed as a hotspot power cross-section in the direction parallel to the BS array, averaged over the location of an intended receiver in the Rx array.

III. Results

A. RT Versus Measurements

By $\hat{\rho}_j$ we denote the correlation function of the RT channel matrix of the virtual array j. Twenty Five environment samples were simulated and in each one $\hat{\rho}_j$ was calculated with (5), in which the correlation matrices of the channels are given by (1). Similarly, by ρ_j^i we denote the correlation function measured in the array A_j^i. Fig. 3 compares ρ in channels obtained from the measured (A_j^l, A_j^l) and simulated $(\hat{A}_j)$ arrays for Δ up to 1.25 m.

The top axis at the Fig. 3 displays Δ in the units of wavelength at 2.61 GHz. In general, all presented functions are decreasing with Δ. The distance to the BS is the primary factor influencing the rate at which the correlation drops.

The measured receiver array pair (A_1^l, A_1^r) is the closest to the BS (2.2 m). ρ_1^l and ρ_1^r are similar and fall off steeper than ρ_2^l and ρ_2^r. They reach their minimum of around 0.12 at $\Delta \simeq 0.6$ m ($\simeq 4\lambda$). ρ_2^l and ρ_2^r both fall more steadily and bottom out at $\Delta \simeq 0.8$ m ($\simeq 5.5\lambda$) at a level of approximately 0.2.

The RT simulations show a very good agreement with measurements, predicting the absolute values and general behavior of the correlation functions. For A_1 arrays the largest absolute error was found at the subwavelength distances, where the RT underestimates the initial drop by around 0.1. The underestimation is slightly higher for A_2 arrays, but unlike the previous case, the largest absolute error of around 0.13 was observed at $\Delta \simeq 0.55$ m. To further quantify the accuracy of the RT method in predicting the correlation function, we performed the least-square fit of the Gaussian function

$$f(\Delta, \sigma) = \exp\left(-\frac{\Delta^2}{2\sigma^2}\right) \tag{6}$$

to ρ_j^r, ρ_j^l and $\hat{\rho}_j$ over parameter σ. By $\sigma(\rho)$ we denote the value of σ obtained after fitting (6) to ρ. We found that $\sigma(\rho_1^l) \simeq \sigma(\rho_1^l) \simeq 0.27$, while $\sigma(\hat{\rho}_1) \simeq 0.25$, which means that the RT estimate relative error was around 8% at 2.2 m distance from the BS. At 3.5 m, $\sigma(\rho_2^l) \simeq 0.39, \sigma(\rho_2^l) \simeq 0.37$, and $\sigma(\hat{\rho}_2) \simeq 0.34$, which resulted in the relative error of around 10%.

B. FS-LOS Versus RT

We constructed the FS-LOS channels of all four RT-simulated receiver arrays, as described in the Section II-C. We denote the correlation function derived from the FS-LOS channel matrix $H_j^{\rightarrow}$ as $\rho_j^{\rightarrow}$. Graphs of $\hat{\rho}_j$ and $\rho_j^{\rightarrow}, j \in \{1, 2, 3, 4\}$ are given at Fig. 4

The FS-LOS correlation functions overestimate the RT at smaller values of Δ and underestimate it for larger Δ. While FS-LOS model predicts a smooth concave fade-out of the correlation with Δ, the full RT simulations show an abrupt drop at $\Delta \leq 1\lambda$, followed by a nearly linear descent at larger Δ. The initial drop at a subwavelength scale increases in magnitude with the Tx–Rx distance: For A_4, it approaches 40%.

IV. Conclusion

In this letter we explore the spatial correlation of the massive MIMO channels with controlled distance between the receivers. We introduced the spatial correlation function as a measure of the average correlation profile in proximity of a given location. The channels measured with the massive MIMO testbed were compared to the simulations using the RT method and the FS-LOS model. The correlation functions calculated from the measured channels were decreasing with the interreceiver distance, with the higher decrease rate, the further the BS to receiver distance was. In general, the RT simulations show a good agreement with measurements, predicting the correlation minima and values. The FS-LOS model was unable to accurately predict the correlation profiles. The obtained results generality is limited by the environment type and scenario in which the measurements were performed. To further validate the presented methodology, future contributions will be focused on other relevant massive MIMO scenarios, e.g., non-LOS at larger BS-UE distances or outdoor-to-indoor links.

REFERENCES

[1] T. L. Marzetta, E. G. Larsson, H. Yang, and H. Q. Ngo, *Fundamentals of Massive MIMO*. Cambridge, U.K.: Cambridge Univ. Press, 2016.

[2] E. Björnson, L. Sanguinetti, H. Wymeersch, J. Hoydis, and T. L. Marzetta, "Massive MIMO is a reality–What is next? Five promising research directions for antenna arrays," *Digit. Signal Process.*, vol. 94, pp. 3–20, 2019.

[3] E. G. Larsson, O. Edfors, F. Tufvesson, and T. L. Marzetta, "Massive MIMO for next generation wireless systems," *IEEE Commun. Mag.*, vol. 52, no. 2, pp. 186–195, Feb. 2014.

[4] J. Choi and D. J. Love, "Bounds on eigenvalues of a spatial correlation matrix," *IEEE Commun. Lett.*, vol. 18, no. 8, pp. 1391–1394, Aug. 2014.

[5] C.-M. Chen, V. Volski, L. Van der Perre, G. A. Vandenbosch, and S. Pollin, "Finite large antenna arrays for massive MIMO: Characterization and system impact," *IEEE Trans. Antennas Propag.*, vol. 65, no. 12, pp. 6712–6720, Dec. 2017.

[6] S. Claessens, C.-M. Chen, D. Schreurs, and S. Pollin, "Massive MIMO for SWIPT: A measurement-based study of precoding," in *Proc. IEEE 19th Int. Workshop Signal Process. Adv. Wireless Commun.*, 2018, pp. 1–5.

[7] S. Shikhantsov *et al.*, "Hybrid ray-tracing/FDTD method for human exposure evaluation of a massive MIMO technology in an industrial indoor environment," *IEEE Access*, vol. 7, pp. 21 0 20–21 031, 2019.

[8] S. Shikhantsov *et al.*, "Massive mimo propagation modeling with user-induced coupling effects using ray-tracing and FDTD," *IEEE J. Sel. Areas Commun.*, vol. 38, no. 9, pp. 1955–1963, Sep. 2020.

[9] X. Gao, J. Flordelis, G. Dahman, F. Tufvesson, and O. Edfors, "Massive MIMO channel modeling-extension of the COST 2100 model," in *Proc. Joint NEWCOM/COST Workshop Wireless Commun.*, 2015, 4558–4563.

[10] A. O. Martinez, E. De Carvalho, and J. Ø. Nielsen, "Massive MIMO properties based on measured channels: Channel hardening, user decorrelation and channel sparsity," in *Proc. 50th Asilomar Conf. Signals, Syst. Comput.*, 2016, pp. 1804–1808.

[11] J. Weng, X. Tu, Z. Lai, S. Salous, and J. Zhang, "Indoor massive MIMO channel modelling using ray-launching simulation," *Int. J. Antennas Propag.*, vol. 2014, 2014, Art. no. 279380.

[12] F. Mani, F. Quitin, and C. Oestges, "Directional spreads of dense multipath components in indoor environments: Experimental validation of a ray-tracing approach," *IEEE Trans. Antennas Propag.*, vol. 60, no. 7, pp. 3389–3396, Jul. 2012.

[13] J. Li, "LOS probability modeling for 5G indoor scenario," in *Proc. Int. Symp. Antennas Propag.*, 2016, pp. 204–205.

[14] F. Voigtländer *et al.*, "5G for the factory of the future: Wireless communication in an industrial environment," 2019, *arXiv:1904.01476*.

[15] S. K. Rao and R. Prasad, "Impact of 5G technologies on industry 4.0," *Wireless Pers. Commun.*, vol. 100, no. 1, pp. 145–159, 2018.

[16] M. Aleksy, F. Dai, N. Enayati, P. Rost, and G. Pocovi, "Utilizing 5G in industrial robotic applications," in *Proc. 7th Int. Conf. Future Internet Things Cloud*, 2019, pp. 278–284.

[17] D. Mills, J. Martin, J. Burbank, and W. Kasch, "Network time protocol version 4: Protocol and algorithms specification," Internet Eng. Task Force, Fremont, CA, USA, RFC 5905, 2010.

[18] D. Dunbar and G. Humphreys, "A spatial data structure for fast poisson-disk sample generation," *ACM Trans. Graph.*, vol. 25, no. 3, pp. 503–508, 2006.

[19] REMCOM, State College, PA, USA, *Wireless InSite 3.2.0 Reference Manual*, 2017. [Online]. Available: http://www.remcom.com/WirelessInSite